

Fermi Level and Light Driven Defect Generation in Silicon Solar Cells

Andrew Diggs^{‡,*}, Zitong Zhao^{‡,†}, Adam Goga, Zachary Crawford, and Gergely T. Zimányi

Physics Department, University of California

Davis, CA 95616, USA[‡]

(Dated: January 11, 2025)

Hydrogenated amorphous silicon (a-Si:H) has had a long standing role as a passivating dielectric for c-Si, often utilized in the early development of ICs and more recently for Si solar cells. Although it has been studied for more than 60 years, several questions about the material properties remain open, including light-induced degradation and the Fermi level dependence on the mobility of hydrogen. Here we study the origin of these phenomenon using electronic structure based calculations. First, we use density functional theory (DFT) and the nudged elastic band (NEB) method to examine defect generation via Si-H bond breaking in p-type, intrinsic, and n-type a-Si:H. We find that the energy barrier controlling this defect generation, shows the same asymmetric reduction of ~ 0.3 eV for p-type and ~ 0.1 eV for n-type, observed in experimental studies. We then develop a model based on the local Coulomb interactions at the transition state, which provides compelling evidence that the asymmetry results from the emergence of a high energy donor state created by the interstitial H. Finally, we repeat our Si-H bond breaking analysis, combining NEB with constrained density functional perturbation theory (c-DFPT) to simulate defect generation dynamics in illuminated a-Si:H. Here we find that e-p pair results in a combined effect that reduces the barrier by ~ 0.4 , in close agreement with experimental observations.

I. INTRODUCTION

Silicon heterojunction (Si HJ) solar cells are part of the promising “next generation” Si solar cells, which utilize a passivating contact cell designs. Si HJ currently hold the efficiency record for single crystal non-concentrator Si solar cell, at 27.3% [1], largely due to their unmatched open circuit voltage (V_{oc}). A key driver for their performance is the excellent electronic passivation of the c-Si absorber by a thin layer of intrinsic hydrogenated amorphous silicon below the doped contact layer. In spite of their great promise, fielded modules have shown an initial degradation of $\sim 0.7\%$ per yr [2], much higher than the usual rate of 0.2% per yr [3]. The excess 0.5% per yr rate was attributed to the degradation of the open circuit voltage V_{oc} [2, 3], which has been linked to the loss of passivating hydrogen [4]. Therefore, understanding and subsequently minimizing the performance loss of Si HJ solar cells is key to accelerating their market acceptance.

Amorphous silicon has had a long standing role as a passivating dielectric, often utilized in the early development of ICs. Although it has been studied for more than 60 years, several questions about the material properties remain open, such as understanding the classes of structural and electronic defects, their formation and statistical distributions, and the long-term structural dynamics. A comprehensive review of these issues was compiled by N. M. Johnson in 1991 [5], and more recent reviews of these issues specifically relating to solar cells are those by S. DeWolf 2012 [6] and C. Wronski 2014. [7]

One of the more intriguing unresolved issues is light induced degradation in intrinsic amorphous silicon, commonly referred to as the Staebler-Wronski effect (SWE). In 1977 Staebler and Wronski

* amdiggs@ucdavis.edu

† ztzhao@ucdavis.edu

‡ These two authors contributed equally to this work.

found that after prolonged light exposure, intrinsic a-Si:H underwent a loss of the dark conductivity. This degradation was fully reversible through dark annealing. It was suggested that the decrease in the dark conductivity is due to a decrease in the thermal free carrier density which is strongly linked to the Fermi level. The drop in the conductivity/Fermi level was attributed to an increase in midgap states [8]. This phenomenon has been the focus of many studies over the last 50 years [9–15]; however, to this date there remains no agreed upon theory for the light induced degradation in a-Si:H. Many speculate that the primary driver of light induced degradation (LID) is generation of Si DB through the loss of hydrogen [16, 17].

This intuition has driven many studies to focus on the kinetics of hydrogen in a-Si:H. Specifically, large efforts have been made to understand the influence of illumination and forward bias injection, Fermi level, and electric fields on the mobility of hydrogen in a-Si:H [14, 16, 18–25].

From these studies additional mysterious and unresolved phenomena emerged, involving the charge state of mobile hydrogen and the influence of the Fermi level on the mobility of hydrogen. Figure 1a shows a well known result from the works of W. Beyer in 1991, who found that the effusion, and thus diffusion, of hydrogen is asymmetrically increased for doped a-Si:H, with a larger increase for p-type and a smaller increase for n-type [18]. Following these results, additional studies directly measured the diffusion of H in doped a-Si:H. These studies determined the energy barrier controlling hydrogen diffusion, and found a remarkable ~ 0.3 eV decrease in p-type a-Si:H and a ~ 0.1 eV decrease in n-type a-Si:H, relative to intrinsic a-Si:H. Additionally, compensated a-Si:H, B + P doped, showed almost no change in the mobility of H compared to intrinsic a-Si:H. The similar behaviors in intrinsic and compensated samples indicated that the change in hydrogen mobility was not tied to specific interactions with the dopant atoms but a direct result of the Fermi level [18–20, 26, 27]. The connection between hydrogen mobility and Fermi level sparked numerous efforts exploring this topic, many of which focused on the charge state of hydrogen as a possible explanation for this phenomenon [25, 27–29]. Recently this topic has reemerged after a similar phenomenon was observed regarding the degradation of the V_{oc} in Si HJ solar cells. The results of one of these studies is shown in Fig. 1b, where a significant difference was found between the thermal degradation in n-type (lower) and p-type (higher) symmetrically passivated Si HJ stacks [30].

All of these issues play a crucial role in the passivation and degradation of the crystalline/amorphous interface of Si HJs [31–33]. The primary form of degradation seen in Si HJ cells has been attributed to an increase in surface recombination at the c-Si/a-Si:H interface. Here, dangling bonds (DBs) are thought to be the primary recombination centers [15]. In a previous SolDeg study we developed a comprehensive model for the thermally driven degradation resulting from the loss of passivating hydrogen resulting in an increase of the DB density at the c-Si/a-Si:H interface [4]. As a natural continuation of that work we have carried out a comprehensive first principals computational investigation of the influence of the Fermi level and photo-excited carriers on the mobility of hydrogen and defect generation in Si HJ. Specifically, we looked at defect generation via Si-H bond breaking in p-type, intrinsic, and n-type crystalline and amorphous Si. We found that near an available Si DB defect state, the lowest energy interstitial site for H in all types is the Si-Si bond center (BC), and that this bond center hydrogen (BCH) creates a high energy state near the conduction band tail which acts as an electron donor. Additionally, we determined the energy barriers controlling this defect generation, where we found the same asymmetric reduction of ~ 0.3 eV for p-type and ~ 0.1 eV for n-type, compared to intrinsic Si. Furthermore, we found that the changes in these barriers can be well explained by the local Coulomb interactions, and that the asymmetry arises from the emergence of the BCH donor state. Finally, we repeat our Si-H bond breaking analysis, using constrained density functional perturbation theory (c-DFPT) to simulate electron-hole pairs generated by illumination. Here we find that the electronic configuration is such that the barrier

gets the combined effect of both the p-type and n-type cells, resulting in a total reduction of ~ 0.4 , which is in agreement with previously reported experiment results [16].

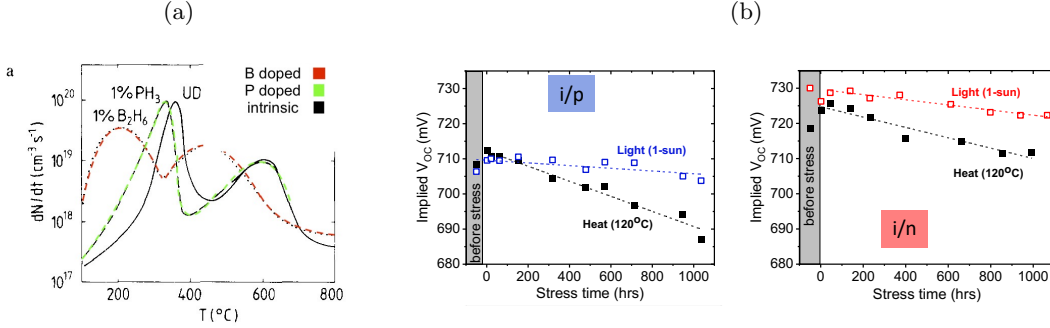


FIG. 1: Experimental results showing the difference in hydrogen kinetics in a-Si:H and Si HJ. **a)** The effusion and diffusion of H in a-Si:H shows asymmetrical increases for p-type and n-type samples relative to intrinsic. Reproduced from W. Beyer *J. Non-Cryst. Solids* (1989). **b)** The thermal degradation in Si HJ stacks is noticeably different for n/i/n and n/i/p stacks. Courtesy of Ujjwal Das and Margaret Zeile IEC-University of Delaware.

II. DEFECT GENERATION DYNAMICS IN CRYSTALLINE AND AMORPHOUS SILICON

We extended our SolDeg platform to study the local and global effects of the Fermi level on defect generation in silicon heterojunction solar cells by combining MD, DFT, full device simulations, and kinetic modeling. To carry out this large-scale investigation, simultaneous studies using DFT were conducted, one using a plain wave basis and the other using a Gaussian basis. Gaussian basis calculations were performed in the CP2K suite, using a Perdew-Burke-Ernzerhof (PBE) [34] exchange correlation functional (E_{xx}) and a Goedecker-Teter-Hutter (GTH) pseudopotential (PP). These calculations were performed to extend our capabilities to the ~ 400 atom c-Si/a-Si:H stacks created in our previous study [4], and to see if/how the contrasting localizing tendencies of the two basis sets might affect the results.[35] Unless stated otherwise, the results presented here were performed using a plane wave basis in the Quantum Espresso (QE) suite [36, 37] using a PBEsol E_{xx} [38] and a projector augmented wave (PAW) PP [39, 40]. Additional plane wave calculations were performed using a PBE0 hybrid functional with 0.25 exact exchange [41], as well as Hubbard corrected density functional theory, with and without inter-site corrections (DFT+U+V)/(DFT+U) using a PBE E_{xx} and a norm conserving PP [42–44].

A. Defect Formation Kinetics in Doped c-Si

We started this study by exploring the effect of the Fermi level on defect formation in c-Si. To do this, we started with a $2 \times 2 \times 2$ (5.43\AA)³ c-Si super cell containing 64 Si. One Si was removed, leaving four DB which were then passivated with hydrogen, resulting in a super cell containing 63

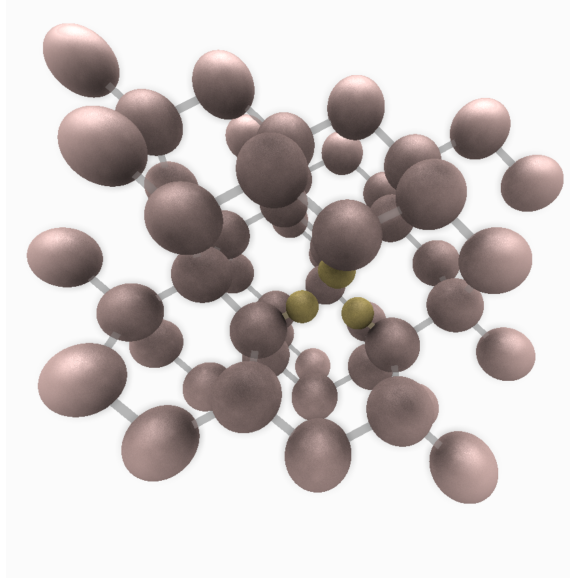


FIG. 2: The initial structure used in this part of our work was a 63 Si + 4 H containing a fully passivated Si vacancy.

Si and 4 H, shown in Fig 2. A similar structure using a $3 \times 3 \times 3$ (5.43\AA)³ c-Si cell containing 215 Si and 4 H were used for additional calculations to check for finite size effects.

To set the Fermi level in a simulation we used two methods: First, we added dopent atoms; specifically, B, nothing, P, or B+P, to create p-type, intrinsic, n-type, and compensated cells. Second, we varied the total super cell charge by subtracting or adding one electron from the neutral super cell, resulting in three cells with total cell charge $Q = +q_e, 0, -q_e$, representing p-type, intrinsic, and n-type c-Si. For clarity, in our notation the charge of an electron is given as $-q_e$. Thus, adding one electron results in a total cell charge $Q = -q_e$, and subtracting one electron, adding a hole, results in a cell with total cell charge $Q = +q_e$. Early in this study we found close correspondence between both methods. For the sake of simplicity the results presented here will be for the charged cell calculations only, unless stated otherwise. For specific results comparing both methods see Supplementary Materials.

To obtain our final defect-free initial cells, we performed a variable cell relaxation using BFGS optimization to an energy tolerance of $10^{-4}Ry$ and a force tolerance of $10^{-3}Ry$. Self consistent field (scf) calculations were performed using a kinetic energy cutoff of 50.0 Ry for wavefunctions and 400.0 Ry for charge density, with a convergence threshold of 10^{-8} . K point sampling was done using a $4 \times 4 \times 4$ Monkhorst-Pack grid centered at (0, 0, 0) for the 67 atom super cell, and a $2 \times 2 \times 2$ Monkhorst-Pack grid centered at (0, 0, 0) for the 219 atom super cell. All parameters were established through convergence to an error tolerance of < 0.1 meV per atom.

In our previous work we created defects by displacing a hydrogen from a Si-H bond to a next nearest neighbor Si-Si BC, which had been reported to be the most stable interstitial site for hydrogen in intrinsic Si [25, 45], and was confirmed by our simulations. However, it has been reported that the lowest energy configuration for interstitial H is dependent on the Fermi level [25]. Based on an informed decision [4, 25, 46, 47] we explored the three most likely interstitial

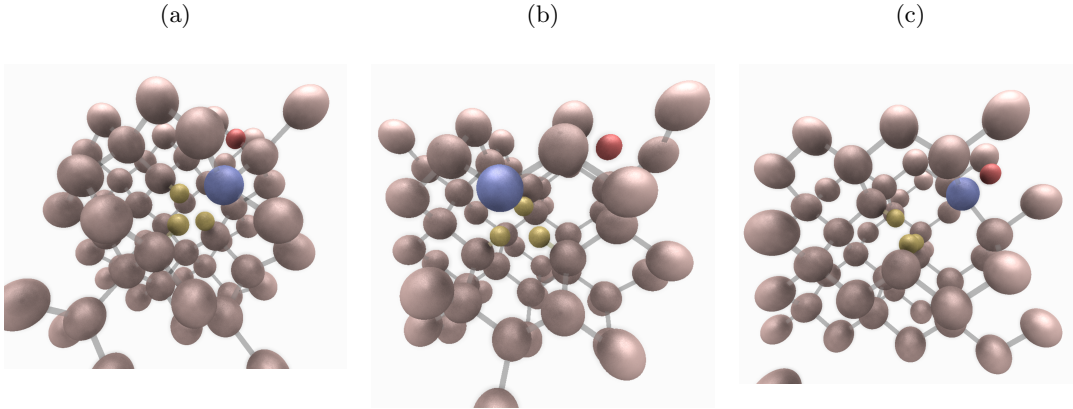


FIG. 3: Three interstitial hydrogen configurations, **(a)** Si-Si BC, **(b)** tetrahedral center, and **(c)** the anti-bonding site, were tested for all three super cell charges $+q_e, 0, -q_e$, to establish the Fermi level dependent defect configuration. In agreement with previous work, for p-type and intrinsic, $+q_e$ and 0, the Si-Si BC was the lowest energy defect configuration. In defect-free c-Si the tetrahedral center was lowest energy configuration for n-type, $-q_e$ [25, 46]. However, near the vicinity of a Si DB, the lowest energy configuration in the n-type cell shifted to a Si-Si BC.

configurations: the Si-Si bond center, the tetrahedral center, and anti-bonding site (AB), shown in Fig. 3. All three interstitial sites were tested for each Fermi level. Additionally, we carried out the same procedure in defect-free, 64 Si + H, intrinsic and n-type cells.

In all cells we found that the AB site was the lowest in energy. However, consistent with previous work [48], we found that this configuration was only meta-stable and did not result in any recombination active defects. In the p-type and intrinsic cells, the Si-Si BC was the lowest energy interstitial defect configuration for hydrogen, which agreed with previous studies [4, 25, 45]. Previous works reported that for n-type Si the tetrahedral position was the lowest energy interstitial site for H [25]. In the n-type cells, we found that the tetrahedral center was the lowest energy interstitial configuration for the defect-free cell; however, with a Si DB present, the lowest energy configuration shifted to the Si-Si BC. We will henceforth refer to these Si-H-Si bond centered hydrogen as (BCH) complexes.

B. Identifying Recombination Active Defects

After finding the lowest energy configuration for interstitial hydrogen in our simulation cells we proceeded to determine the electronic properties of these configurations. To do this we computed the density of states projected onto the atomic orbital basis (PDOS), as implemented in QE. By projecting the DOS onto the atomic orbital basis we can directly discern the contribution of each individual atom to a state. A fully delocalized state contains contribution from many atoms, thus the projection should be small, $\sim \frac{1}{N}$. In contrast a localized state will have large contribution from only a few atoms. This is the same principal used for determining defects with the IPR. This technique allowed us to track the change in defect states between our initially fully passivated

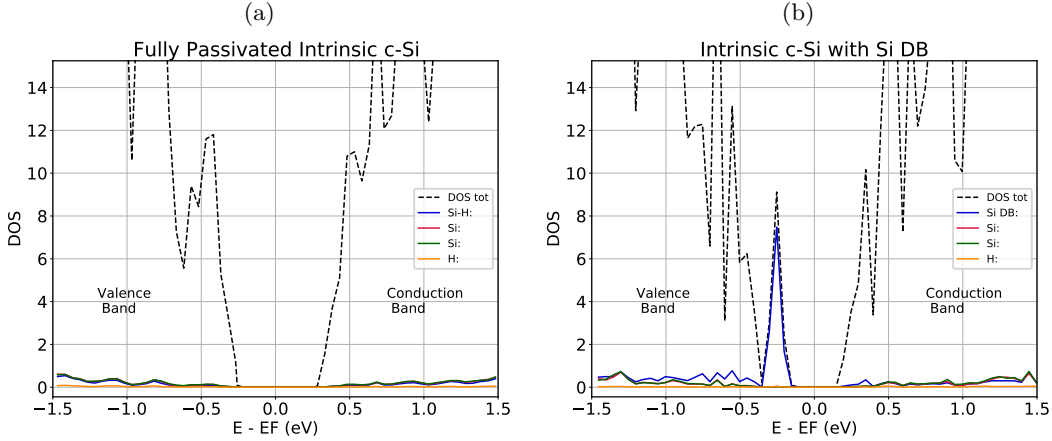


FIG. 4: The projected density of states for **(a)** the fully passivated c-Si cell which shows an uninterrupted bandgap indicating no electronic defects. The delocalized states are made from small contributions by many atoms, thus the density of a Si in these states (blue, red, and green lines) is much smaller than the total density of states (dashed black line). **(b)** After the Si-H bond breaks a defect state appears in the bandgap. The projections show that this defect state is almost entirely localized on the Si DB (blue line). The states below the Fermi level are the occupied states. Unexpectedly for intrinsic Si, the Si DB is occupied by two electrons.

cells and our final cells containing one Si DB and one interstitial H, as well as determine the contributions to defect states by individual atoms. Figure 4 shows that in the fully passivated c-Si cell the bandgap is uninterrupted, thus no electronic defects are present. In the final configuration a midgap defect state appears, and it is almost entirely localized on the Si DB.

One entirely unexpected result came out of our defect analysis. In Fig. 4 the state of the Si DB is the state for one electron with degeneracy of two. For a spin symmetric calculation, only the lower half of the Si DB state would be occupied if the Si DB was occupied by one electron. This would result in a computed Fermi level, halfway between HOMO and LUMO, in the middle of the DB states. Figure 4 shows that in the final configuration the Fermi level is between the DB states and the conduction band, indicating that the DB is in fact occupied by two electrons.

C. The Si-H-Si Donor State

The Si DB is well known to be a deep amphoteric defect, meaning it can have three different occupations/charge states: empty, $1e^-$, and $2e^-$ with corresponding charge $q_{DB} = +q_e, 0$, and $-q_e$. The energy of $q_{DB} = +q_e, 0$ charge states ($E_{DB_{+/0}}$) is near midgap, showing a negative charge transition level, $E_{DB_-} = \epsilon_{DB_{+/0}} + U$, with a reported correlation energy $U \approx 0.2$ eV [29, 49, 50]. For a defect of this nature one would expect the ground state occupation to follow [51]

$$q_{DB} = \begin{cases} +q_e & E_F < \epsilon_{DB_{+/0}} \\ 0 & \epsilon_{DB_{+/0}} < E_F < \epsilon_{DB_-} \\ -q_e & E_F > \epsilon_{DB_-} \end{cases} \quad (1)$$

After observing the unexpected double occupation of the Si DB in the our defect structures, we proceeded to clarify these results prior to proceeding with our investigation into defect generation dynamics.

We began our “extra charge” analysis by exploring the occupation of the DB without a BCH complex present. To do this we started with the initial fully passivated cell, from which one H was removed, leaving behind a Si DB. We then relaxed three cells using a variable cell relaxation with the three cell charges, and computed the PDOS and the Löwdin population. We found that without a BCH complex nearby, the occupations of the Si DB follow the expected Fermi-Dirac statistics, shown in Fig. 5. We also computed the effective dangling bond charge, q_{DB} , which is the difference between the Löwdin population of the Si DB and the average Löwdin population of the other Si in the super cell. We found that q_{DB} , reported in Table I, tracked well with the occupations provided by the PDOS, granting us additional insight into the local electronic configurations.

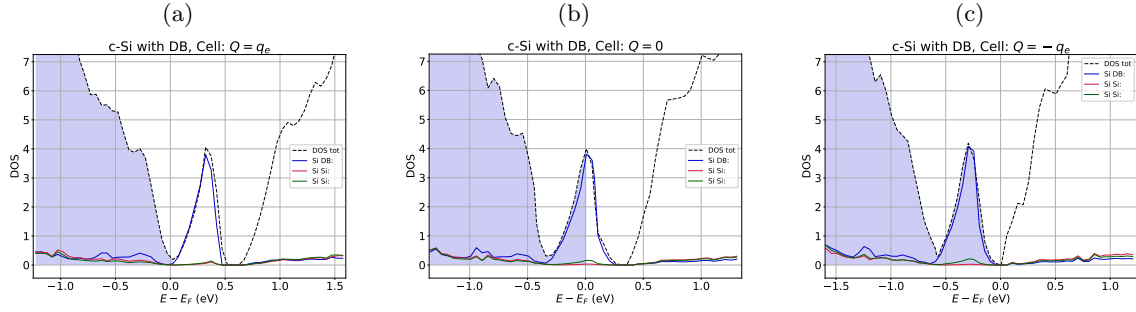


FIG. 5: The projected density of states for our three 63 Si + 3 H super cells with total cell charges a) $Q = +q_e$, b) $Q = 0$, and c) $Q = -q_e$. In the absence of a BCH complex the DB occupation is as expected.

Cell Charge	q_{DB}
$+q_e$	0.149
0	-0.037
$-q_e$	-0.208

TABLE I: Löwdin population of Si DB for super cell charges $Q = q_e, 0, -q_e$

After establishing the occupation of the DB without a BCH complex, we turned our attention to the electronic structure of a BCH complex without a Si DB. To do this we placed one H in otherwise perfect c-Si, then computed the PDOS and Löwdin population. We found that even in an otherwise perfect crystal the BCH complex creates a high energy state near the conduction band minimum.

Here we point out that determining the precise energy of this state relative to the CBM in c-Si is problematic with the computational methods used in this work. A well known problem with semi-local DFT is the underestimation of the bandgap of many materials [52]. For Si, DFT predicts the bandgap of ~ 0.6 eV compared to experimentally determined 1.13 eV. Thus, the placement of the BCH state in the conduction band tail could be due to the under estimation of the bandgap. Additionally, experiments have shown the Si DB to have a $0/-$ charge transition of ~ 0.2 eV, i.e. $U \sim 0.2$ eV. Our our study thus far did not include Hubbard corrections; therefore, the relative energy difference between the BCH state and the negative Si DB could be in error. To eliminate, to the best of our ability, any method based faulty results, we conducted a substantial additional computational effort including DFT/LSDA+U, DFT+U+V, and hybrid functional calculation with PBE0 [41–44], details of which can be found in Supplementary Materials. These efforts were informative and supported our findings using standard DFT; however, the additional computational cost made continuing with these methods prohibitive. Therefore, we continued our study using the initial methods described earlier.

After validating our methods we were confident to conclude that: (1) a BCH complex creates a localized high energy state near the CBM, (2) this state is higher in energy than the energy states of the Si DB.

With our newfound insight we returned to our study of the three defect structures containing a Si DB and a BCH complex. For each of these cells, we computed the electronic properties using our same PDOS and the Löwdin population analysis. Figure 6 shows the PDOS and Table II reports the q_{eff} for these calculations, revealing our first key finding of this work. We found that, in the vicinity of an available Si DB state, the BCH acts as a donor and an electron easily spills over into the lower energy state of the DB. Thus the occupation of the Si DB is now representative of the doping/cell charge, plus an additional donor. Further, the PDOS in Fig. 6 shows that the BCH state is primarily made up by the two BCH Si, BC_a and BC_b , and the H barely contributes, if at all. Our calculated q_{eff} corroborates this, which shows that in all three cell charges the hydrogen atom in the BCH complex is essentially neutral, and the charge that has long been associated with an interstitial H atom is in fact that of the nearby Si, with a large portion localized on the two Si of the BCH complex. In the presence of an electric field a charged H would directly experience an additional force driving its motion. However, for the charged BCH complex the additional force will mostly be felt by the two BCH Si, which are not highly mobile. Our results showing a charged BCH complex are consistent with experimental results that found that changes in the mobility of H in an external electric field were not consistent with the picture of a charged hydrogen atom [21, 22].

III. DEFECT GENERATION DYNAMICS IN DOPED C-SI

After determining the unique electronic structure resulting from the interaction between a BCH complex and an adjacent Si DB, we returned to the initial focus for this work: the asymmetric enhancement in the mobility of hydrogen in doped a-Si:H and its connection to the observed degradation in silicon heterojunction stacks. The next step in our SolDeg method was to determine the energy barriers controlling defect generation. To do this, we again turned to the nudged elastic band method; specifically, we used c-NEB as implemented in QE. For the initial image we used our fully passivated 63 Si + 4 H cells, and for the final image we used the final defect configuration cells containing a Si DB and a BCH. We used 7 total images, resulting in 5 intermediate images which created a path connecting the initial and final images.

To find the MEP we took a three step approach. First, the 5 intermediate images were relaxed

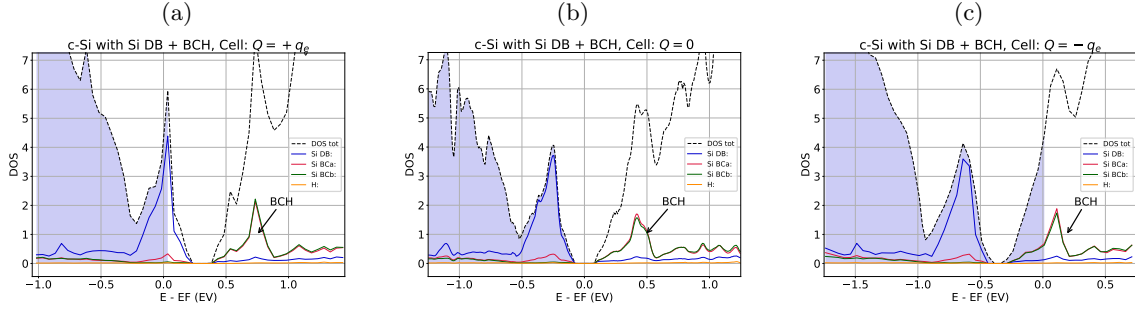


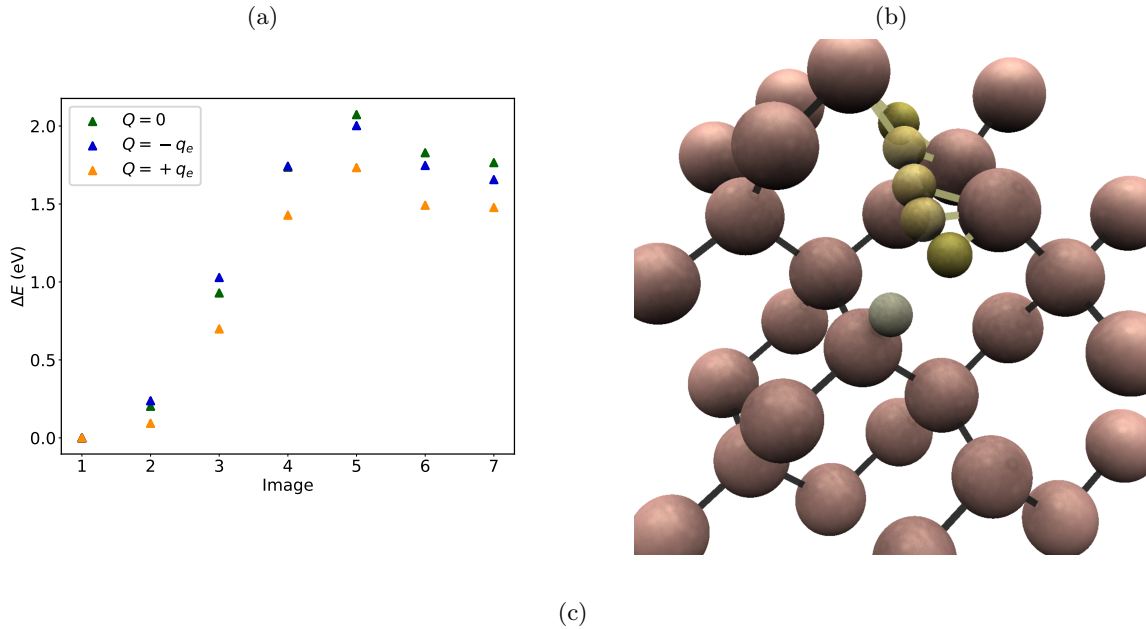
FIG. 6: The projected density of states for c-Si with one Si DB and one BCH complex for three super cell charges: a) $Q = +q_e$, b) $Q = 0$, and c) $Q = -q_e$. With an adjacent BCH complex, the occupation of the Si DB reflects that of the cell charge plus a donor.

Cell Charge, Q	q_H	q_{db}	q_{BCa}	q_{BCb}	q_{BCH}
$+q_e$	-0.030	-0.055	0.191	0.200	0.362
0	-0.039	-0.177	0.184	0.192	0.338
$-q_e$	-0.034	-0.186	0.146	0.151	0.263

TABLE II: q_{eff} for the key atoms in the final defect state: the interstitial H, q_H , the Si DB, q_{DB} , the two Si in the BCH complex, q_{BCa} , q_{BCb} , and the BCH complex, q_{BCH} . Strikingly, q_H remains almost constant and is essentially neutral for all cell charges. For cell charges $+q_e$ and 0, q_{DB} is occupied by the electron donated by the BCH complex. In all three cells q_{BCH} carries a large positive charge; however, the change in q_{BCH} between the intrinsic cell and the n-type cell is $0.075 q_e$, which shows that a large amount of the additional e is localized on the BCH, compared to the $\frac{1}{N} \sim 0.015$ for a delocalized electron.

using BFGS optimization with no climbing images to a path tolerance of $0.1 \text{ eV}/\text{\AA}$. If convergence was achieved, the resulting path was used to restart the NEB calculation, with the highest energy image set as a climbing image and now using a path tolerance of $0.09 \text{ eV}/\text{\AA}$. [53] Finally, if convergence was reached for the climbing image run, that path was used to restart the NEB calculation keeping the same climbing image but now using a path tolerance of $0.05 \text{ eV}/\text{\AA}$. This full procedure was carried out individually for our p-type, intrinsic, and n-type cells.

The computed barriers and the corresponding MEPs are reported in Table 7c and shown in Fig. 7a respectively. These findings represent the second key result of this work. We find that the computed energy barriers for our p-type, intrinsic, and n-type cells show the same asymmetric reduction as those predicted by experimental observations [18, 20, 27].



Cell Charge	E_{BB} (eV)	E_{recap} (eV)
$+q_e$	1.73	0.26
0	2.07	0.31
$-q_e$	1.98	0.35

FIG. 7: **(a)** Minimum energy paths energy barriers for Si-H bond breaking in our p-type, intrinsic, and n-type cells. **(b)** Shows the corresponding atomic motion of the H along the MEP. **(c)** Gives the corresponding values for the energy barriers. Remarkably we find the same asymmetric reductions for our doped cells as reported by experiment.

A. Zero Point Energy Correction

According to TSS the rate of a reaction, k^\ddagger , is given by the probability that a reactant A reaches the TS multiplied by the flux through the TS

$$k^\ddagger = \frac{\mathcal{Z}^\ddagger}{\mathcal{Z}^A} v^\ddagger \quad (2)$$

where $\mathcal{Z}^\ddagger/\mathcal{Z}^A$ are the partition functions of the TSS/reactants, and v^\ddagger is the reaction coordinate velocity through the TS [48, 54, 55]. For a quantum system near the ground state, an important correction to the $\mathcal{Z}^\ddagger/\mathcal{Z}^A$ term in Eq. 2 is the difference in the zero point energies of the thermal partition functions (ΔE_{ZP}). ΔE_{ZP} is commonly computed using using the first order approximation

$$\Delta E_{ZP} = \sum_n \frac{1}{2} \hbar \omega_n^\ddagger - \sum_m \frac{1}{2} \hbar \omega_m^A \quad (3)$$

where ω^\ddagger/ω^A are the phonon frequencies at the transition state and initial state respectively. We computed the phonon spectrum for the initial, transition, and final state using *phonon* package in QE, and then calculated Eq. 3 for both the forward and reverse barriers using all real frequencies. Due to the substantial computational expense, this was done for the intrinsic cell only; however, ΔE_{ZP} should be roughly similar in the doped cells. Table III shows our computed ΔE_{ZP} and the corrected Si-H bond breaking barriers, which now align closely with previously reported values [4, 20, 26].

Barrier	ΔE_{ZP} (eV)	Corrected Barrier (eV)
$E_{forward}$	-0.632	1.44
$E_{reverse}$	0.053	0.36

TABLE III: ΔE_{ZP} and the corrected energy barriers for Si-H bond breaking in intrinsic c-Si.

B. The Origin of The Fermi Level Dependence of Si-H Bond Breaking

After reproducing the experimentally observed asymmetric change in the Si-H bond breaking barrier with regard to the Fermi level, we proceeded to determine the underlying physics responsible for this phenomena. We recalled from our analysis of the BCH complex that the occupation of the Si DB showed a similar asymmetry, in that it was doubly occupied in both the intrinsic and n-type cells, while only singly occupied in the p-type cell. Motivated by these observations we proceeded to explore the occupations and localized charge density at the transition state. To do this, we computed the PDOS and q_{eff} of the transition state structure, given by the saddle point configuration of the NEB path.

Cell Charge	q_H	q_{DB}	q_{BC_a}	q_{BC_b}	q_{BCH}	ΔE_C
q_e	0.085	-0.029	0.109	0.048	0.231	0.0042
0	0.074	-0.182	0.130	0.059	0.253	0.0068
$-q_e$	0.049	-0.200	0.127	0.066	0.232	0.0051

TABLE IV: q_{eff} for the atoms locally involved in the Si-H bond breaking process: the H, q_H , the newly formed Si DB, q_{DB} , the two BCH Si, q_{BC_a} and q_{BC_b} , and the whole BCH complex, q_{BCH} . ΔE_C is the local change in the Coulomb energy for these atoms at the transition state.

The PDOS at the TS are shown in Fig. 8 and the corresponding q_{eff} are reported in Table IV; together they represent our third key finding. We found that at the TSS a precursor to the high energy state of the BCH complex had emerged. However, unlike the final BCH state, this state showed a substantial contribution from the H. The emergence of this state created a high energy electron that spilled over into the lower energy state of Si DB, after which the occupation of the Si DB transitioned to extra donor filling observed in the final configurations. This analysis was further supported by our q_{eff} calculations. Comparing the results presented in Table IV to those presented in Table II, we found that q_{DB} showed very similar values at both the TSS and the final state. At the TSS, q_{BC_a} is slightly lower than at the final state, and q_{BC_b} is now close to neutral in contrast

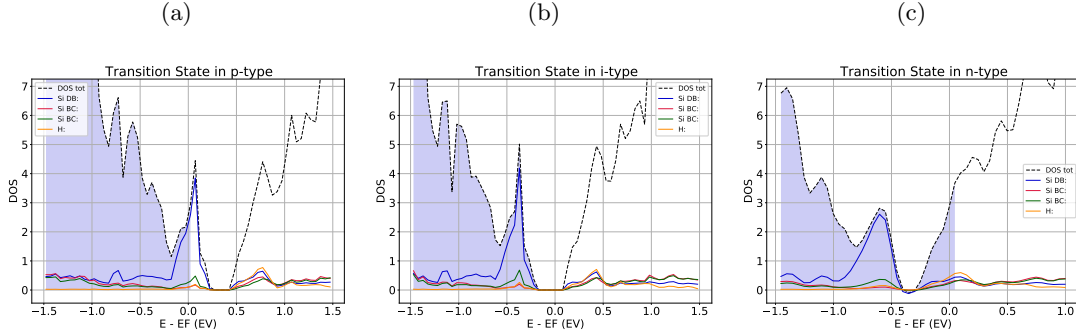


FIG. 8: The projected density of states at the transition state of the Si-H bond breaking process for a) p-type, b) intrinsic, and c) n-type super cells.

to its substantial positive charge shown at the final state. The most substantial difference seen was in q_H , which at the TSS is now positive and noticeably larger in the p-type and intrinsic cells than in the n-type cell. Combining these results we developed a hypothesis that the change in the Si-H bond breaking barrier was the result of changes in the local Coulomb interactions along the MEP. In the p-type cell the q_H is largest but $q_{DB} \sim 0$, therefore the product $q_H * q_{DB}$ is small. In the intrinsic cell q_H is large and positive and q_{DB} is large and negative, thus the product $q_H * q_{DB}$ is large and negative, indicating a strong attraction. In the n-type cell q_{DB} is large and negative but the additional electron reduces q_H , which reduces the product $q_H * q_{DB}$, thus decreasing the attractive force. For a qualitative measure of this effect we determined the change in the Coulomb energy, ΔE_C , between the initial image and the TSS image along the adiabat corresponding to q_{eff} of the TSS. Specifically we computed

$$\Delta E_C = q_H \left(\frac{q_{DB}}{\Delta r_{DB}} + \frac{q_{BC_a}}{\Delta r_{BC_a}} + \frac{q_{BC_b}}{\Delta r_{BC_b}} \right). \quad (4)$$

ΔE_C for our three different Fermi levels is reported in Table IV, which shows a markedly similar asymmetry to the energy barriers. These findings support our model, where the Fermi level dependence of Si-H bond breaking is the result of changes in the local Coulombic interactions between the Si DB and the BCH complex.

C. Interstitial Hydrogen Dynamics in Doped c-Si

In our previous work we found that Si-H bond breaking was only one part of the total mechanism controlling hydrogen motion in Si [4]. In that work we found that the ratios of the barriers controlling the recapture of a hydrogen by a Si DB, E_{recap} , the hopping out of the first Si BC into the next, E_{drift} , and the reverse of that process, E_{return} , had a substantial effect on the overall kinetics. To investigate similar effects we computed the energy barriers controlling the hopping of a H in a BCH to an adjacent Si-Si BC. This was done using the same NEB procedures outlined in the previous section. The computed “next BC” hopping barriers, along with the Si-H bond breaking barriers, are reported in Table V. Using a set of coupled rate equations we computed an effective bond breaking barrier. The computed effective barriers showed only small variations from the Si-H

bond breaking barriers. Thus, in absence of a density gradient the Si-H bond breaking barrier is a sufficient measure of the energy barrier controlling hydrogen kinetics, and thus defect generation, in crystalline and amorphous silicon.

Super Cell Charge	E_{BB} (eV)	E_{recap} (eV)	E_{drift} (eV)	E_{return} (eV)
$+q_e$	1.73	0.26	0.26	0.36
0	2.07	0.31	0.28	0.36
$-q_e$	1.98	0.35	0.31	0.33

TABLE V: Energy barriers determined by NEB for Si-H bond breaking and next BC hopping for our p-type, intrinsic, and n-type cells. There are slight differences in the next BC hopping barriers for the different cells; however, our computed effective barriers showed only slight variations from the Si-H bond breaking barrier. Therefore, the Si-H bond breaking barrier is a sufficient measure of the thermal barrier that controls H motion in amorphous and crystalline Si.

IV. DEFECT GENERATION DYNAMICS IN DOPED A-SI:H

After determining the mechanisms responsible for the changes in the Si-H bond breaking barrier, and therefore the barrier controlling hydrogen motion, in c-Si we proceeded to investigate how these findings might change due to the macroscopic differences, e.g., bandgap, and the microscopic differences, e.g., strained bonds, micro-voids, and other BCH, in a-Si:H. We began by creating a-Si:H super cells of roughly the same size to keep computational costs lower and to remain consistent with finite size effects such as localized charge-jellium interactions.

The a-Si:H structures were created with classical MD using the LAMMPS simulator [56] with our previously developed Si:H GAP interatomic potential [57]. We began by creating c-Si structures with randomly distributed vacancies and hydrogen atoms to achieve initial structures with densities of 2.28, 2.23, and 2.19 g/cm³ with 15 at% hydrogen. In accordance with our previous work, we used a validated melt-quench method, first heating the cell to 1800K to form liquid Si:H, followed by a quench to 1500K at a rate of 10¹³Ks⁻¹. The cells were then allowed to equilibrate for 100 ps using canonical, NVT, sampling with a Nosé-Hoover thermostat. This was followed by a second quench to 500K at a rate of 10¹²Ks⁻¹ using isothermal-isobaric, NPT, sampling with a Nosé-Hoover thermostat. Finally the cells were relaxed using a Hessian free truncated Newtonian optimization to a convergence tolerance of 10⁻³. In some cells additional H were added to passivate Si DBs that interfered with our desired calculations. Specifically, in some cells, two Si DBs that were spatially separate, i.e., not part of the same micro-void, were able to interact through the periodic boundaries and form a band, thus delocalizing the occupying electrons. Prior to DFT calculations, all cells were relaxed with DFT using a variable cell relaxation with BFGS optimization to an energy tolerance of 10⁻⁴ Ry and a force tolerance of 10⁻³ Ry.

We carried out the same SolDeg procedure as was used for the c-Si: We created defects by displacing a H from an Si-H bond, computed the barriers controlling defect creation, then analyzed the electronic properties of the initial, transition state, and final structures. This was also done for doped, compensated, and charged cells. The results of our a-Si:H study were for the most part consistent with our results in c-Si. There were, however, some unique results that needed to be considered to construct a reliable model for Si-H bond breaking in a-Si:H. We found that in all cases where a hole was present at an energy lower than the Si DB, a similar $\sim 0.2 - 0.3$ eV reduction as

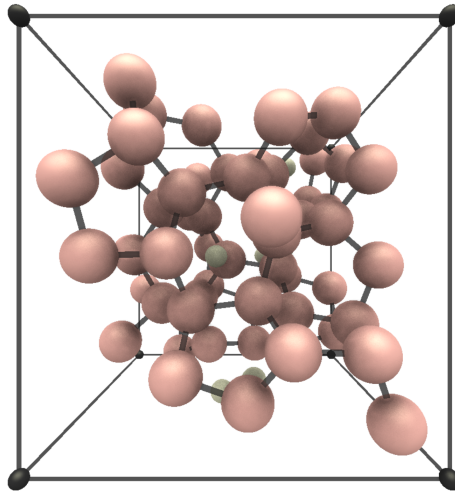


FIG. 9: Example a-Si:H super cell containing 61 Si and 9 H, 15 at% H.

was found in our p-type c-Si cell occurred in the Si-H bond breaking barrier. However, due to the variability of bonding configurations in the a-Si:H, the energy of the Si DB sometimes fell into the valence band tail and the barrier reduction was diminished or lost altogether. In the n-type a-Si:H cells a similar effect was seen, regarding the energy state of the BCH complex and the conduction band. Figure 10 shows the PDOS for two different final BCH configurations in our n-type a-Si:H cells. In Fig 10a the BCH complex state lies in the bandgap, and thus is highly localized. With this configuration, at the TSS the extra electron is much more localized on the BCH precursor state, which further reduces the barrier. In some case we found the Si-H bond breaking barrier was lowered by as much as 0.15 eV compared to 0.8 eV observed in the c-Si. On the other hand, Fig. 10b shows that sometimes the BCH complex state was located completely within the conduction band and the barrier reduction was lost all together.

These effects are caused by the distribution of bonding configurations in the a-Si:H, and thus the energy states of the Si DB and the BCH complex will be similarly distributed. Thus, at a given Fermi level the distributions of the energy states will have different occupations resulting in different bond breaking barriers. To model these effects requires distributions of energy levels for both Si DB and BCH in a-Si:H. Collecting large enough data sets to build up distributions was cost- and time-prohibitive; however, in our previous work we showed that the Si-Si and Si-H bond lengths [33], as well as the Si-H bond breaking barriers [4] were both Gaussian distributed. It is therefore reasonable to expect that the energy positions of the DB and BCH are also Gaussian distributed. Using the mean values of the energy levels relative to the valence band maximum for the Si DB, $\bar{E}_{DB} = 0.4$ eV, and the BCH complex, $\bar{E}_{BCH} = 0.85$ eV, obtained in this work, we constructed Gaussian distributed E_{DB} and E_{BCH} that were used to compute the average Si-H bond breaking barrier as a function of the Fermi level, using our NEB computed barriers with the ZPE correction. Figure 11 shows the results of our SolDeg-modeled effective bond breaking barrier next to the experimentally determined barriers controlling hydrogen diffusion in c-Si, μ c-Si, and a-Si:H [26] as a function of the Fermi level. The compelling match between our model and experiment represents the fourth key finding of this work. The results of this work provide a consistent theory

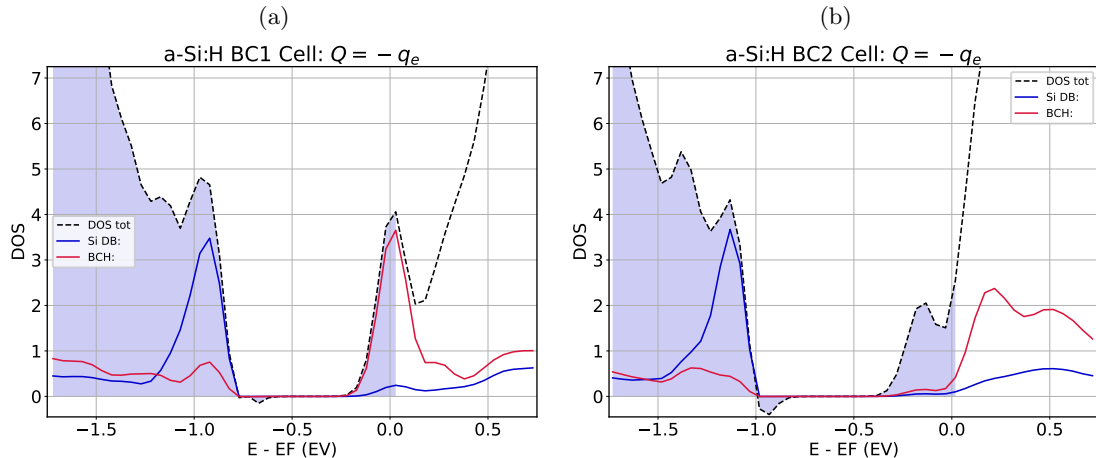


FIG. 10: The projected density of states for the Si DB and the combined BCH complex in n-type a-Si:H with two different final defect structures. **(a)** The BCH complex state falls below the conduction band. This allows the extra charge to better stabilize the charged BCH complex at the TSS thus further reducing the Si-H bond breaking barrier. **(b)** The BCH complex state is completely within the conduction band and the barrier reduction is lost all together.

for the observed Fermi level dependence of hydrogen mobility and defect generation in a-Si:H.

V. LIGHT-INDUCED DEFECT GENERATION IN C-SI

After determining the mechanism responsible for the Fermi level dependence of Si-H bond breaking in silicon and developing a model for $E_{BB}(E_F)$ in a-Si:H that closely matched with experimental results, we turned our focus to the effects of photo-excited carriers on hydrogen mobility and defect generation in c-Si and a-Si:H.

To do this we used constrained density functional perturbation theory, (c-DFPT), to perform two chemical potential calculations that simulate photoexcited carriers by removing n electrons from the valence manifold and constraining them to occupy the conduction manifold, following the work of Marini and Calandra [58]. Figure 12 shows the PDOS for our intrinsic cell in the final Si DB + BCH defect state using the two chemical potential method. As shown by the blue fill, there is a hole in the valence states, accompanied by an electron, red fill, in the conduction states. After developing protocols for the two chemical potential calculations that reliably provided our desired electronic occupations, we proceeded to compute the Si-H bond breaking barriers for n-type, intrinsic, and p-type cells under illumination. For these calculations the cell charge method did not work because the valence manifold was not computed correctly. To carry out calculations of doped c-Si under illumination, we replaced one of the Si atoms in our fully passivated 63 Si + 4 H super cell with either a B or a P, thereby giving us p-type, intrinsic, and n-type cells. Each of these cells was relaxed using a variable cell relaxation with two chemical potentials, constraining one electron in the p-type and intrinsic cells, and two electrons in the n-type cell, into the conduction manifold[59]. Using the relaxed cells we displaced one H to a next nearest neighbor Si-Si BC, followed by a fixed cell relaxation. We then proceeded to compute the Si-H bond breaking barrier for these cells,

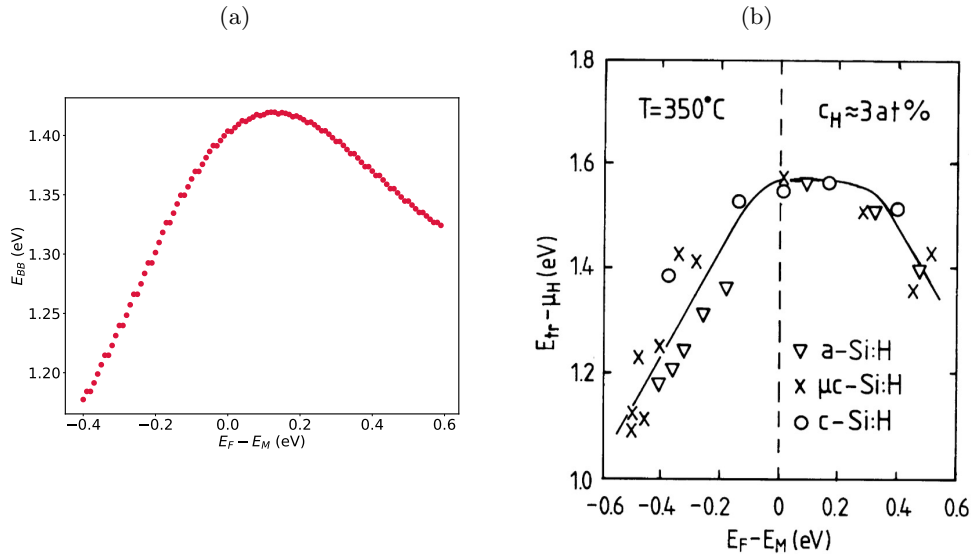


FIG. 11: (a) The average Si-H bond breaking barrier as a function of the Fermi level relative to midgap determined by this work, side by side with (b) the transport energy barrier, E_{tr} , for H diffusion in doped a-Si:H (Δ), c-Si (\circ), and μc -Si (X). Reproduced from the legendary W. Beyer *Solar Energy Materials & Solar Cells*, **78** (2003).

using NEB combined with simulated illumination. We again used a chain of 7 images with the fully passivated cell as the initial image and the Si DB + BCH complex as the final image. The intermediate images were relaxed to a path tolerance of 0.1 eV/Å. Table VI provides the results of these calculations along with our earlier “dark” results for comparison. We find a substantial drop between 0.3-0.4 eV for all the Si-H bond breaking barriers, compared to their dark values. The reduction of 0.47 eV for the intrinsic barrier is in strong agreement with previously reported values [16].

Type	Dark		Light	
	E_{BB} (eV)	E_{recap} (eV)	E_{BB} (eV)	E_{recap} (eV)
p-type	1.73	0.26	1.41	0.23
intrinsic	2.02	0.31	1.60	0.23
n-type	1.93	0.35	1.58	0.25

TABLE VI: Energy barriers for Si-H bond breaking in our p-type, intrinsic, and n-type cells in the dark and under simulated illumination using the two chemical potential method. The dark energy barriers reported here are those obtained using the same path tolerance and no climbing image, to match the parameters used for the illuminated runs.

We followed these NEB calculations with our same PDOS and Löwdin analysis; however, due to computational resources and convergence issues this was done only for the intrinsic cell. Table

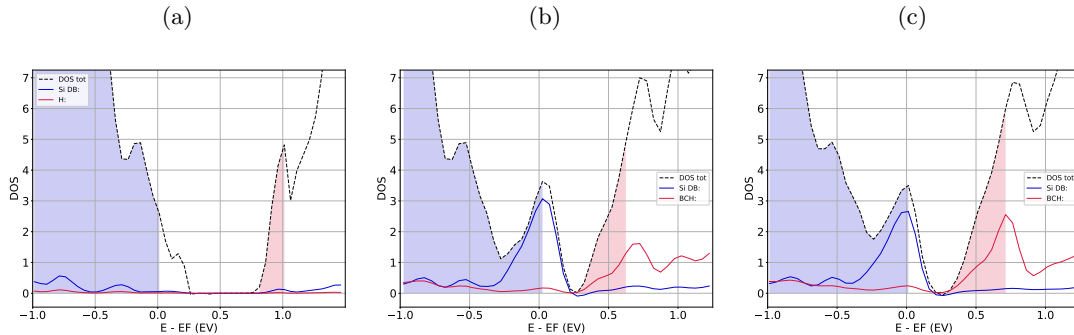


FIG. 12: The projected density of states for 63 Si + 4 H super cell for **(a)** the fully passivated initial image, **(b)** the transition state image, and **(c)** the final defect structure with a Si DB and a BCH complex for our illuminated Si-H bond breaking simulation. To simulate the effects of light we used the two chemical potential method to constrain one electron from the valence band to the conduction band. The blue fill shows the occupied valence states, and the red fill shows the occupied conduction states.

VII shows the results of our q_{eff} calculation, which revealed that in the presence of photo-excited carriers, the TSS[60] gets both of the enhancements we observed in the doped cells: First, the Si-DB is only singly occupied similar to the p-type cell in the dark. Second, the excited carrier occupies the BCH state which helps passivate the H as in the n-type cell in the dark. Combining the two effects reduces the Coulomb energy even further, and thus provides an even greater barrier reduction.

q_H	q_{DB}	q_{BC_a}	q_{BC_b}	q_{BCH}	ΔE_C
0.045	-0.047	0.118	0.080	0.248	0.0031

TABLE VII: Under illumination q_{DB} is close to neutral as in the p-type dark calculation, and q_H is also close to neutral as in the n-type dark calculation. Under illumination both effects are simultaneously achieved providing an even greater reduction to the barrier.

Here we wish to clarify that, in contrast to our earlier calculations, we were unable to obtain convergence with the lower path tolerance or with a climbing image. The TSS used for this calculation is not necessarily the true transition state structure; it is instead, the highest energy image from our non-climbing image NEB. Additionally, it has been shown that photo-excited carriers affect the phonon spectrum in Si [58]. Thus the ZPE correction obtained for our intrinsic cell in the dark is likely not valid. Despite these issues, our results show close correspondence with experimental results [16] and thus reveal the promise of combining the two chemical potential method with NEB to simulate dynamical processes in illuminated systems.

VI. CONCLUSIONS

In this paper we reported on a comprehensive first principals computational study on the effect of the Fermi level and photo-excited carriers on defect generation via Si-H bond breaking in c-Si and a-Si:H. We used density functional theory to study the electronic properties of the atoms locally involved in defect generation, in p-type, intrinsic, and n-type cells both for dark and illuminated conditions.

First, we determined the lowest energy interstitial configuration for hydrogen in our three cells. We found that near a Si dangling bond, the Si-Si bond center was lowest energy configuration even in n-type Si. We found that in these bond center configurations the hydrogen was neutral and the charge delocalized to the neighboring Si. We used NEB to compute Si-H bond breaking barriers at different Fermi levels. We found an asymmetric reduction in the barriers that aligns closely with experimentally reported values. We determined that the change in the local Coulomb energy provided a consistent explanation for the barrier reduction in our doped cells. We performed our Si-H bond breaking analysis in a-Si:H. We found that the distribution of defect energy levels resulted in a distribution of barriers reductions. We computed the effective Si-H bond breaking barrier as a function of Fermi level that matched well to experimental results [26]. Finally, we used the two chemical potential method [58] to simulate the effect of illumination. We found a close correspondence to reported experimental observations, providing support to the method of combining the two chemical potential method with NEB to simulate dynamical process in illuminated materials.

-
- [1] NREL. Best research-cell efficiency chart— photovoltaic research. <https://www.nrel.gov/pv/cell-efficiency.html>, 2024. Accessed: 2024-12-06.
 - [2] Chris Deline, Steve Johnston, Steve R. Rummel, Bill Sekulic, Dirk C Jordan, Steve R Rummel, Peter Hacke, Sarah R Kurtz, Kristopher O Davis, Eric John Schneller, et al. Silicon heterojunction system field performance. *IEEE J. Photovolt*, 8(1):177–182, 2018.
 - [3] Bing Gao, Yahui Shao, Wenzhu Liu, Haitao Xiang, Youlin Yu, and Zhengxin Liu. Out-door reliability and degradation of hit, cigs, n-type multi-busbar, perc, and cdte modules in shanghai, china. *Solar Energy Materials and Solar Cells*, 236:111490, 2022.
 - [4] Andrew Diggs, Zitong Zhao, Reza Vatan Meidanshahi, Davis Unruh, Salman Manzoor, Mariana Bertoni, Stephen M. Goodnick, and Gergely T. Zimányi. Hydrogen-induced degradation dynamics in silicon heterojunction solar cells via machine learning. *Communications Materials*, 4(1), apr 2023.
 - [5] N.M. Johnson, C. Doland, F. Ponce, J. Walker, and G. Anderson. Hydrogen in crystalline semiconductors: A review of experimental results. *Physica B: Condensed Matter*, 170(1):3–20, 1991.
 - [6] Stefaan De Wolf, Antoine Descoeur, Zachary C Holman, and Christophe Ballif. High-efficiency silicon heterojunction solar cells: A review. *green*, 2(1):7–24, 2012.
 - [7] Christopher R. Wronski and Xinwei Niu. The limited relevance of swe dangling bonds to degradation in high-quality a-si:h solar cells. *IEEE Journal of Photovoltaics*, 4(3):778–784, 2014.
 - [8] C.R. Wronski. Chapter 10 the staebler-wronski effect. In Jacques I. Pankove, editor, *Hydrogenated Amorphous Silicon*, volume 21 of *Semiconductors and Semimetals*, pages 347–374. Elsevier, 1984.
 - [9] S. Olibet, Evelyne Vallat, and Christophe Ballif. Effect of light induced degradation on passivating properties of a-si:h layers deposited on crystalline si. 01 2006.
 - [10] M. Stutzmann, W. B. Jackson, and C. C. Tsai. Light-induced metastable defects in hydrogenated amorphous silicon: A systematic study. *Phys. Rev. B*, 32:23–47, Jul 1985.
 - [11] S. R. Elliott. Photo-induced changes in glow-discharge-deposited amorphous silicon: The staebler-wronski effect. *Philosophical Magazine B*, 39(4):349–356, 1979.
 - [12] Richard S. Crandall. Defect relaxation in amorphous silicon: Stretched exponentials, the meyer-neldel

- rule, and the staebler-wronski effect. *Phys. Rev. B*, 43:4057–4070, Feb 1991.
- [13] Jimmy Melskens, Marc Schouten, Awital Mannheim, Albert S. Vullers, Yalda Mohammadian, Stephan W. H. Eijt, Henk Schut, Takuya Matsui, Miro Zeman, and Arno H. M. Smets. The nature and the kinetics of light-induced defect creation in hydrogenated amorphous silicon films and solar cells. *IEEE Journal of Photovoltaics*, 4(6):1331–1336, 2014.
- [14] R. Biswas, Qiming Li, B. C. Pan, and Y. Yoon. Mechanism for hydrogen diffusion in amorphous silicon. *Phys. Rev. B*, 57:2253–2256, Jan 1998.
- [15] Stefaan De Wolf, Christophe Ballif, and Michio Kondo. Kinetics of *a*-si:h bulk defect and *a*-si:h/*c*-si interface-state reduction. *Phys. Rev. B*, 85:113302, Mar 2012.
- [16] P. V. Santos, N. M. Johnson, and R. A. Street. Light-enhanced hydrogen motion in *a*-si:h. *Phys. Rev. Lett.*, 67:2686–2689, Nov 1991.
- [17] Pratish Mahtani, Renaud Varache, Bastien Jovet, Christophe Longeaud, Jean-Paul Kleider, and Nazir P. Kherani. Light induced changes in the amorphous—crystalline silicon heterointerface. *Journal of Applied Physics*, 114(12):124503, 09 2013.
- [18] W. Beyer. Hydrogen effusion: a probe for surface desorption and diffusion. *Physica B: Condensed Matter*, 170(1):105–114, 1991.
- [19] W. Beyer. Incorporation and thermal stability of hydrogen in amorphous silicon and germanium. *Journal of Non-Crystalline Solids*, 198-200:40–45, 1996. Proceedings of the Sixteenth International Conference on Amorphous Semiconductors - Science and Technology.
- [20] R. A. Street, C. C. Tsai, J. Kakalios, and W. B. Jackson. Hydrogen diffusion in amorphous silicon. *Philosophical Magazine B*, 56(3):305–320, 1987.
- [21] P. V. Santos, N. M. Johnson, and R. A. Street. Enhanced hydrogen diffusion under illumination in hydrogenated amorphous silicon. *MRS Online Proceedings Library*, 258:353–358, 1992.
- [22] Paulo V. Santos, N. M. Johnson, R. A. Street, M. Hack, R. Thompson, and C. C. Tsai. Hydrogen migration and electronic carriers in *a*-si:h. *Phys. Rev. B*, 47:10244–10260, Apr 1993.
- [23] J. Kakalios, R. A. Street, and W. B. Jackson. Stretched-exponential relaxation arising from dispersive diffusion of hydrogen in amorphous silicon. *Phys. Rev. Lett.*, 59:1037–1040, Aug 1987.
- [24] A van Wieringen and N Warmholtz. *Physics*, 22, 849 (1956); rc frank and je thomas, jr. *J. Phys. Chem. Solids*, 16:144, 1960.
- [25] Conyers Herring, N. M. Johnson, and Chris G. Van de Walle. Energy levels of isolated interstitial hydrogen in silicon. *Phys. Rev. B*, 64:125209, Sep 2001.
- [26] W Beyer. Diffusion and evolution of hydrogen in hydrogenated amorphous and microcrystalline silicon. *Solar Energy Materials and Solar Cells*, 78(1):235–267, 2003. Critical review of amorphous and microcrystalline silicon materials and solar cells.
- [27] N. H. Nickel and I. E. Beckers. Hydrogen migration in doped and undoped polycrystalline and microcrystalline silicon. *Phys. Rev. B*, 66:075211, Aug 2002.
- [28] J Zhu, NM Johnson, and C Herring. Negative-charge state of hydrogen in silicon. *Physical Review B*, 41(17):12354, 1990.
- [29] Chris G Van de Walle. Energies of various configurations of hydrogen in silicon. *Physical Review B*, 49(7):4579, 1994.
- [30] U. K. Das and Margaret Zeile. Correlating voc degradation with hydrogen evolution kinetics in silicon heterojunction stacks. In *Proc. of the 52nd Photovoltaic Specialist Conference*. Institute of Electrical and Electronics Engineers, 2024.
- [31] Simone Bernardini and Mariana I. Bertoni. Insights into the degradation of amorphous silicon passivation layer for heterojunction solar cells. *phys. status solidi (a)*, 216(4):1800705, 2019.
- [32] Jakub Holovský, Silvia Martín De Nicolás, Stefaan De Wolf, and Christophe Ballif. Amorphous/crystalline silicon interface stability: Correlation between infrared spectroscopy and electronic passivation properties. *Adv. Mater. Interfaces*, 7(20):2000957, 2020.
- [33] Davis Unruh, Reza Vatan Meidanshahi, Chase Hansen, Salman Manzoor, Stephen M. Goodnick, Mariana I. Bertoni, and Gergely T. Zimanyi. From femtoseconds to gigaseconds: The soldeg platform for the performance degradation analysis of silicon heterojunction solar cells. *ACS Appl. Mater. Interfaces*, 13:32424–32434, 2021.
- [34] John P. Perdew, Kieron Burke, and Matthias Ernzerhof. Generalized gradient approximation made

- simple. *Phys. Rev. Lett.*, 77:3865–3868, 1996.
- [35] Plane waves are highly delocalized, and Gaussians are highly localized.
- [36] P. Giannozzi et al. Quantum espresso: a modular and open-source software project for quantum simulations of materials. *J. Phys.: Condens. Matter*, 21:395502, 2009.
- [37] P. Giannozzi et al. Advanced capabilities for materials modelling with quantum espresso. *J. Phys.: Condens. Matter*, 29:465901, 2017.
- [38] John P. Perdew, Adrienn Ruzsinszky, Gábor I. Csonka, Oleg A. Vydrov, Gustavo E. Scuseria, Lucian A. Constantin, Xiaolan Zhou, and Kieron Burke. Restoring the density-gradient expansion for exchange in solids and surfaces. *Phys. Rev. Lett.*, 100:136406, 4 2008.
- [39] P. E. Blöchl. Projector augmented-wave method. *Phys. Rev. B*, 50:17953–17979, 12 1994.
- [40] Andrea Dal Corso. Pseudopotentials periodic table: From h to pu. *Computational Materials Science*, 95:337–350, 2014.
- [41] Carlo Adamo and Vincenzo Barone. Toward reliable density functional methods without adjustable parameters: The pbe0 model. *The Journal of Chemical Physics*, 110(13):6158–6170, 04 1999.
- [42] S. L. Dudarev, G. A. Botton, S. Y. Savrasov, C. J. Humphreys, and A. P. Sutton. Electron-energy-loss spectra and the structural stability of nickel oxide: An lsd+u study. *Phys. Rev. B*, 57:1505–1509, Jan 1998.
- [43] Vivaldo Leiria Campo and Matteo Cococcioni. Extended dft + u + v method with on-site and inter-site electronic interactions. *Journal of Physics: Condensed Matter*, 22(5):055602, jan 2010.
- [44] Iurii Timrov, Nicola Marzari, and Matteo Cococcioni. Hubbard parameters from density-functional perturbation theory. *Phys. Rev. B*, 98:085127, Aug 2018.
- [45] Chris G. Van de Walle and R. A. Street. Structure, energetics, and dissociation of si-h bonds at dangling bonds in silicon. *Phys. Rev. B*, 49:14766–14769, May 1994.
- [46] Markus Jech, Al-Moatasem El-Sayed, Stanislav Tyaginov, Alexander L. Shluger, and Tibor Grasser. *ab initio* treatment of silicon-hydrogen bond rupture at si/sio₂ interfaces. *Phys. Rev. B*, 100:195302, Nov 2019.
- [47] Sokrates Pantelides, Sanwu Wang, A. Franceschetti, Ryszard Buczko, Massimiliano Di Ventra, Sergey Rashkeev, L. Tsetseris, Matthew Evans, Iskander Batyrev, Leonard Feldman, Dhar Sarit, Kweku McDonald, Robert Weller, Ronald Schrimpf, D.M. Fleetwood, X.J. Zhou, John Williams, Chin-Che Tin, G. Y. Chung, and Lisa Porter. Si/sio₂ and sic/sio₂ interfaces for mosfets – challenges and advances. *Materials Science Forum*, 527-529:935–948, 10 2006.
- [48] Markus Jech. *The Physics of non-equilibrium reliability phenomena*. PhD thesis, TU Wien, 2020.
- [49] Sara Olibet, Evelyne Vallat-Sauvain, and Christophe Ballif. Model for a-si:h/c-si interface recombination based on the amphoteric nature of silicon dangling bonds. *Phys. Rev. B*, 76:035326, Jul 2007.
- [50] Stefaan De Wolf and Michio Kondo. Abruptness of a-si:h/c-si interface revealed by carrier lifetime measurements. *Applied Physics Letters*, 90(4):042111, 2007.
- [51] Fermi-Dirac statistics describe only single electron occupations, and are not valid for double occupations with on-site energy. However, for a ground state configuration E_F is specifically the Fermi energy and given by the HOMO and LUMO [61].
- [52] Danny Broberg, Kyle Bystrom, Shivani Srivastava, Diana Dahliah, Benjamin A. D. Williamson, Leigh Weston, David O. Scanlon, Gian-Marco Rignanese, Shyam Dwaraknath, Joel Varley, Kristin A. Persson, Mark Asta, and Geoffroy Hautier. High-throughput calculations of charged point defect properties with semi-local density functional theory—performance benchmarks for materials screening applications. *npj Computational Materials*, 9:2057–3960, 2023.
- [53] The small reduction in the path tolerance was needed to trigger the initial BFGS cycle.
- [54] Maurice Kreevoy and Donald Truhlar. *Transition State Theory*. John Wiley & Sons, 1986.
- [55] Robert W. Balluffi, Samuel M. Allen, and W. Craig Carter. *Kinetics of Materials*. John Wiley & Sons, 2005.
- [56] A. P. Thompson, H. M. Aktulga, R. Berger, D. S. Bolintineanu, W. M. Brown, P. S. Crozier, P. J. in ’t Veld, A. Kohlmeyer, S. G. Moore, T. D. Nguyen, R. Shan, M. J. Stevens, J. Tranchida, C. Trott, and S. J. Plimpton. LAMMPS - a flexible simulation tool for particle-based materials modeling at the atomic, meso, and continuum scales. *Comp. Phys. Comm.*, 271:108171, 2022.
- [57] Davis Unruh, Reza Vatan Meidanshahi, Stephen M. Goodnick, Gábor Csányi, and Gergely T. Zimányi.

- Gaussian approximation potential for amorphous Si:H. *Phys. Rev. Materials*, 6:065603, Jun 2022.
- [58] Giovanni Marini and Matteo Calandra. Lattice dynamics of photoexcited insulators from constrained density-functional perturbation theory. *Phys. Rev. B*, 104:144103, 10 2021.
- [59] The n-type cell needed two electrons constrained to the conduction manifold to properly simulate illumination. Constraining only one electron to the conduction manifold in the n-type cell simulates the ionized P atom, which is not representative of illumination.
- [60] We were unable to reach convergence for our climbing image NEB calculations with the two chemical potential method. Therefore, this is not necessarily the true transition state structure. This is the highest energy image for our non climbing image runs.
- [61] Chih-Tang Sah and W. Shockley. Electron-hole recombination statistics in semiconductors through flaws with many charge conditions. *Phys. Rev.*, 109:1103–1115, Feb 1958.

Supplementary Material

For our Fermi level dependent Si-H bond breaking calculations we performed several additional calculations to confirm our methods and results. Here we present these calculations. In tables the use of (-) indicates a calculation for which convergence was not obtained.

I. INTERSTITIAL H ENERGY

Table I show the energy for the three hydrogen interstitial locations: Si-Si bond center, tetrahedral, and anti-bonding, for all three super cell charges with a Si DB in the cell. The AB is the lowest energy for all super cell charges; however, this configuration is only meta-stable and does not result in any recombination active defect states, see Fig. 2b. Additionally, the barrier for the H to return to the initial configuration is ~ 1.1 eV, which when compared to the ~ 2.0 eV barrier to migrate to a neighboring BC, makes this path very unlikely. The lowest energy defect creating configuration is the Si-Si BC for all cell types when a Si DB is present. Table II shows the energy of the interstitial H for the $Q = 0$ and $Q = -q_e$ super cells in perfect c-Si. Similar to the work of Herring and Van de Walle [?] we find that the tetrahedral is lowest in energy for the $Q = -q_e$ super cell.

State	$Q = +q_e$	$Q = 0$	$Q = -q_e$
BCH	-535.066558 Ry	-534.61178832 Ry	-534.07363748 Ry
Tetrahedral	-	-534.536213 Ry	-534.04636 Ry
Anti-bonding	-535.163684 Ry	-534.68886373 Ry	-534.1500233 Ry

TABLE I: Relaxed energies for all interstitial H configurations in c-Si with a DB, for $Q = +q_e$, $Q = 0$, and $Q = -q_e$ super cells. Using a $3 \times 3 \times 3$ k point grid, Ecutwfc = 50.

State	$Q = 0$	$Q = -q_e$
Initial	-718.86797 Ry	-718.3902 Ry
BC1	-718.738226 Ry	-718.2659 Ry
BC2	-718.744297 Ry	-718.26927 Ry
Tetrahedral	-718.70922 Ry	-718.25784 Ry
Anti-bonding	-718.8283 Ry	-718.34833 Ry

TABLE II: Relaxed energies for all interstitial H configurations in perfect c-Si, for the $Q = 0$ and $Q = -q_e$ super cells. Using a $3 \times 3 \times 3$ k point grid, Ecutwfc = 50.

II. SI-H BOND BREAKING C-SI

Tables for the Si-H bond breaking barrier in c-Si for both P/B doped and charged cells.

Charge	$\Delta E_{forward}$ (eV)	$\Delta E_{reverse}$ (eV)
B doped	1.77631	0.28931
+1	1.79125	0.2903
0	2.0879	0.3057
-1	2.0056	0.3146
P doped	2.0104	0.3068

TABLE III: Final results for Si-H bond breaking barrier in c-Si comparing doped cell with charged cells. NEB parameters: path tol = 0.1 c-Si with PBESOL EXX and rrkjus PP, with CI.

Charge	$\Delta E_{forward}$ (eV)	$\Delta E_{reverse}$ (eV)
+1	1.732	0.254
0	2.024	0.259
-1	1.925	0.268

TABLE IV: Final results for c-Si, NEB parameters: path tol = 0.1, PBESOL EXX and PAW PP, no CI.

Charge	$\Delta E_{forward}$ (eV)	$\Delta E_{reverse}$ (eV)
+1	1.733	0.255
0	2.073	0.308
-1	1.986	0.346

TABLE V: Final Si-H bond breaking results for c-Si. NEB parameters: path tol = 0.7 with PBESOL EXX and PAW PP, with CI.

A. Zero point energy correction

The reported values in table IX were much higher than the expected values from our previous work, which showed an Si-H bond breaking barrier distribution centered around 1.3 eV. This dis-

Charge	$\Delta E_{forward}$ (eV)	$\Delta E_{reverse}$ (eV)	$\frac{E_f}{E_r}$
+1	0.268	0.364	0.74
0	0.293	0.375	0.78
-1	0.279	0.307	0.91

TABLE VI: Final BC-BC hopping results for c-Si. NEB parameters: path tol = 0.7 with PBESOL EXX and PAW PP, with CI.

tribution was calculated with MD in LAMMPS using SiH GAP potential. We explored various parameters to see what is the cause of the significant difference.

Method	PP/Exc	Opt	Path tol	$\Delta E_{forward}$ (eV)	$\Delta E_{reverse}$
DFT	NC/PBE	BFGS	0.1	2.038154	0.381815
DFT	NC/PBE	BFGS	0.05	2.152296	0.495956
DFT	NC/SLA	BFGS	0.1	1.912620	0.342148
DFT	NC/SLA	BFGS	0.1	1.930685	0.360214
MD	GAP	quick min	10^{-8}	1.33974	0.238787
MD	GAP	quick min	10^{-4}	1.63737	0.51272

TABLE VII: $2.04g/cm^3$ a-Si:H Bond breaking NEB for path 1

One important issue is the zero point energy correction (ΔZPE) to the thermal partition function. In the MD runs a damped dynamics minimization is used that allows for the NEB to be computed at non-zero temperature. For the DFT, the barriers are computed at the ground state; as such, ΔZPE becomes an important contribution to the Z^\ddagger/Z^A term in Eq. ???. ΔZPE is commonly computed using using the first order approximation

$$\Delta ZPE = \sum_n \frac{1}{2} \hbar \omega_n^\ddagger - \sum_m \frac{1}{2} \hbar \omega_m^A \quad (1)$$

where ω^\ddagger/ω^A are the phonon modes at the transition state and initial state respectively. We computed the phonon spectrum for the initial, transition, and final state using *phonon* package in QE. Due to the substantial computational expense, this was done for the intrinsic cell only.

Barrier	ΔZPE
$E_{forward}$	-0.632 eV
$E_{reverse}$	0.053 eV

TABLE VIII: ΔZPE for Si-H bond breaking in intrinsic c-Si.

III. SI-H BOND BREAKING IN A-SI:H

After determining the converged parameters were proceeded to compute the Si-H bond breaking barrier and BC-BC hopping barrier in several a-Si:H cells with varying mass density. We again used both B/P doped and charged cells.

Charge/Doping	$\Delta E_{forward}$ (eV)	$\Delta E_{reverse}$	E_F
(i-type) Q=0	2.03815	0.381815	5.4157
(n-type) P Doped	2.028300	0.389923	5.6806
(i-type) Q=-1	2.031770	0.41056	5.7991
(p-type) B Doped	1.974865	0.325204	4.8233
(i-type) Q=+1	2.014568	0.332619	4.870

TABLE IX: $2.04g/cm^3$ a-Si:H Bond breaking NEB for path 1, No CI.

Charge/Doping	E Final (Ry)	E_F (eV)	HOMO (eV)	LUMO (eV)
(i-type) Q=0	-457.1622 Ry	5.0172	4.5610	5.2700
(n-type) P Doped	-462.5518 Ry	4.9339	4.9287	4.9339
(p-type) B Doped	-454.5006 Ry	4.6862	4.6740	4.7203
(i-type) Q=+1	-457.5061 Ry	4.7405	4.7365	4.7775
(i-type) Q=-1	-456.7921 Ry	4.8956	4.8954	4.9004

TABLE X: $2.00g/cm^3$ a-Si:H initial structure relaxation.

Charge/Doping	$\Delta E_{forward}$ (eV)	$\Delta E_{reverse}$
(i-type) Q=0	2.14533	0.615198
(n-type) P Doped	2.2219	0.6465
(i-type) Q=-1	2.204095	0.640397
(p-type) B Doped	2.177966	0.541463
(i-type) Q=+1	2.189911	0.537928

TABLE XI: $2.00g/cm^3$ a-Si:H Bond breaking NEB, No CI.

Charge/Doping	$\Delta E_{forward}$ (eV)	$\Delta E_{reverse}$
(i-type) Q=0	-	-
(n-type) P Doped	0.64235	0.878876
(p-type) B Doped	0.619591	1.083476
(i-type) Q=+1	0.639572	1.062325
(i-type) Q=-1		

TABLE XII: $2.00g/cm^3$ a-Si:H BC-BC Hop NEB , No CI.

End	Charge	$\Delta E_{forward}$ (eV)	$\Delta E_{reverse}$ (eV)
BC1	0	2.320	0.680
BC1	-1	2.332	0.651
BC1	+1	-	-
BC1	+2	2.042	0.549
BC1	BNQ	2.270	0.653
BC2	0	2.184	0.909
BC2	-1	2.038	0.949
BC2	+1	2.278	0.846
BC2	+2	2.093	0.813
BC2	BNQ	2.141	0.920
BC3	0	2.093	0.479
BC3	-1	2.060	1.185
BC3	+1	2.027	0.411
BC3	+2	1.780	0.362
BC3	BNQ	2.054	0.466
BC4	0	2.074	0.807
BC4	-1	2.176	1.078
BC4	+1	2.252	0.970
BC4	+2	1.840	1.197
BC4	BNQ	2.129	0.891

TABLE XIII: Si-H NEB barriers for $2.18 g/cm^3$ a-Si:H, H44 using DFT+U with PBE Exx and NC PP

End	Charge	$\Delta E_{forward}$ (eV)	$\Delta E_{reverse}$ (eV)
BC1	0	2.139	0.625
BC1	$+q_e$	1.916	0.553
BC1	$-q_e$	2.026	0.642
BC2	0	2.047	0.720
BC2	$+q_e$	1.830	0.624
BC2	$-q_e$	2.034	0.706
BC3	0	1.790	0.089
BC3	$+q_e$	1.522	0.064
BC3	$-q_e$	1.736	0.139
BC4	0	1.697	0.646
BC4	$+q_e$	1.464	0.693
BC4	$-q_e$	1.642	0.908

TABLE XIV: 2.21 g/cm^3 a-Si:H, Si-H NEB barriers for $Q = +q_e$, $Q = 0$, and $Q = -q_e$. Using PBEsol E_{xx} with PAW PP.

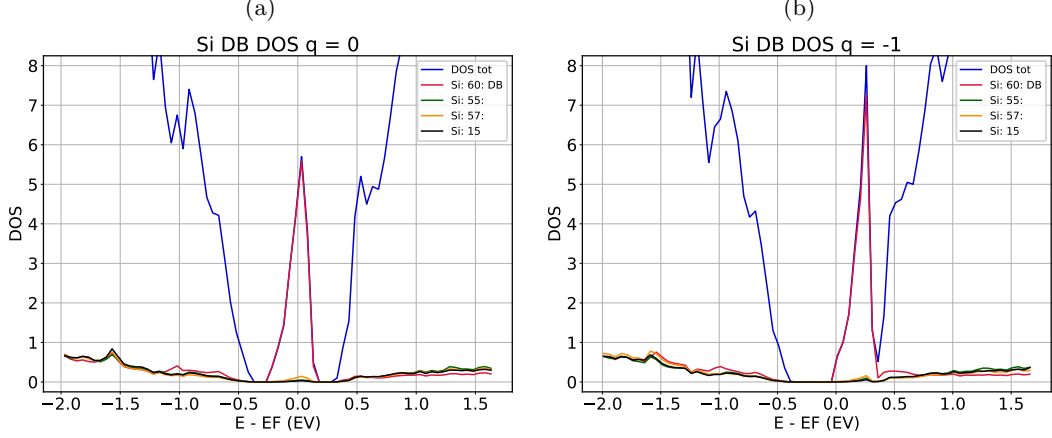


FIG. 1: Using the computed U the Si DB **(a)** occupied by one electron is near mid gap **(b)** occupied by two electrons shifts the peak of the DB energy ~ 0.2 eV, which is consistent with reported values.

IV. DFT+U/ DFT+U+V

DFT+U+V uses the extended Hubbard model to add on-site and inter-site corrections to DFT.

$$H_{Hub} = \sum_{ij\sigma} t_{ij} c_{i\sigma}^\dagger c_{j\sigma} + U \sum_i n_{i\uparrow} n_{i\downarrow} \pm \sum_{ij\sigma\sigma'} V_{ij} n_{i\sigma} n_{j\sigma'} \quad (2)$$

These corrections greatly improve localization.

A. Computing U and $U+V$ with RPA

The first Step is to compute U and V . This is done using DFPT to compute the linear response matrix in the random phase approximation.

$$\chi_{RPA} = \frac{\chi_0}{1 - U\chi_0} \quad (3)$$

Which when inverted gives U on the diagonal and V on the off diagonal. For 67 atom super cell there are 201 irreducible representations. The wall time for HP calculation was 36h56m43.52s.

Different H configurations using DFT + U with NC PP and PBE Exc, and using U Si-3p = 1.427, U H-1s = 6.36. Computed using hp.x

Different H configurations using DFT + $U + V$ with NC PP and PBE Exc, and using U Si = 1.427, U H = 6.360, V Si-Si = 0.210, V Si-H = 0.313

After gaining confidence with DFT+ $U+V$, we proceeded to compute the Si-H bond breaking barriers. The use of Hubbard corrections slightly enhances the effect of the Fermi level on the barriers. Each configuration and atom type requires a full χ_{RPA} calculation which scales as $N^3 \ln(N)$. The continued use of DFT+ $U+V$ was not realistic for this reason.

H configuration	Total Charge	E_{tot}	E_{F}	E_{U}
DB	0	-533.57177431 Ry	6.3661 eV	2.82749 Ry
DB	-1	-533.06820708 Ry	6.4336 eV	2.883298 Ry
BCH	0	-534.61178832 Ry	6.3612 eV	2.87437757 Ry
BCH	-1	-534.07363748 Ry	6.6565 eV	2.947886 Ry
Anti-bond	0	-534.68886373 Ry	6.3615 eV	2.89003340 Ry
Anti-bond	-1	-534.1500233 Ry	6.7380 eV	2.95298 Ry
Tetrahedral	0	-534.536213 Ry	6.09336 eV	2.91630647 Ry
Tetrahedral	-1	-534.04636Ry	6.2505 eV	2.96175407 Ry

TABLE XV: BCH vs Tetrahedral H With $q = 0$ and $q = -1$ super cell using DFT+U+V.

Charge	$\Delta E_{\text{forward}}$ (eV)	$\Delta E_{\text{reverse}}$ (eV)
+1	2.1539	0.4956
B doped	2.1979	0.4989
0	2.3840	0.4410
-1	2.3062	0.5137
P doped	2.3059	0.4724

TABLE XVI: Results for c-Si with 3x3x3 super cell no CI with PBE-NC and +U. CI did not converge for these calculations

V. SUPPORTING FIGURES

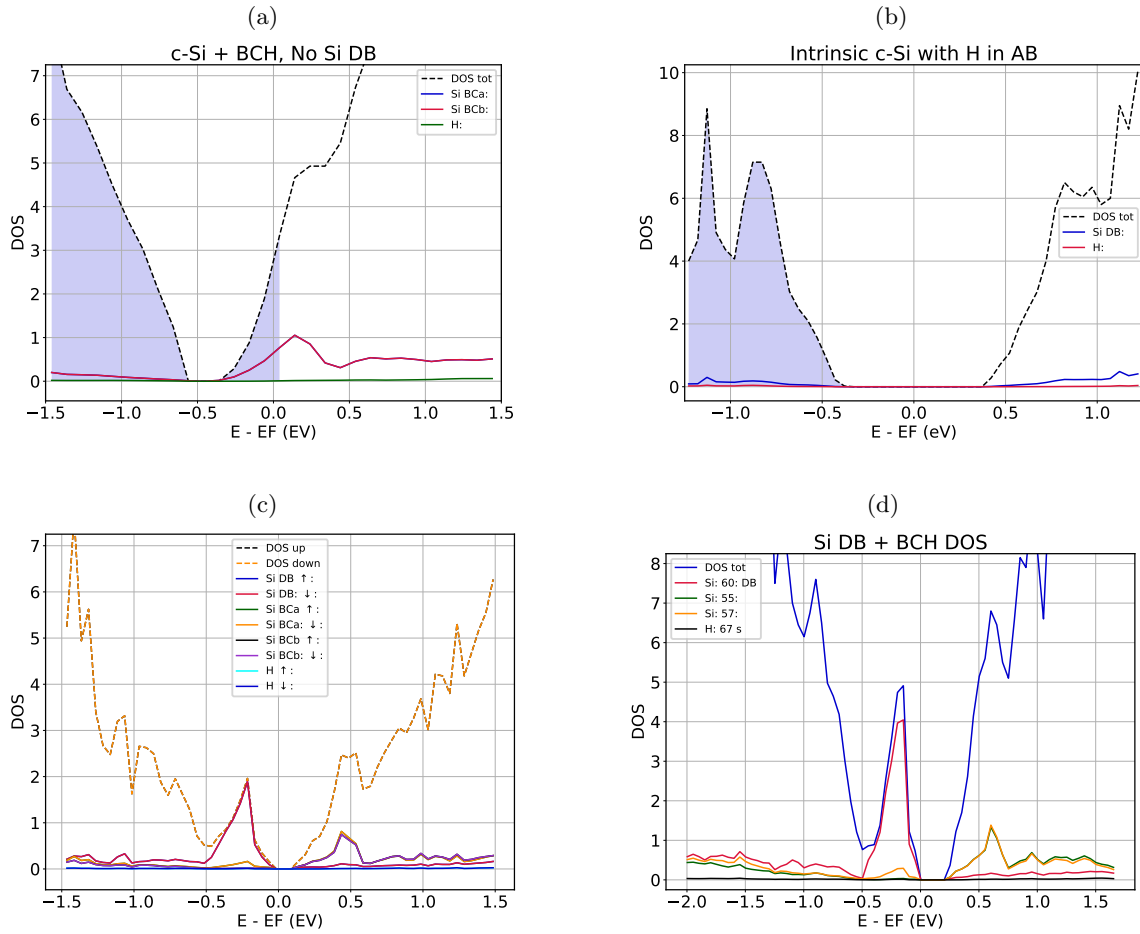


FIG. 2: **(a)** PDOS of perfect c-Si with a BCH complex. The state is in the exact same place but it is now occupied due to the lack of a Si DB at lower energy. **(b)** PDOS for c-Si with a Si DB and the H at the AB interstitial site. The AB configuration is meta-stable and does not produce a mid-gap state. **(c)** Si DB + BCH final state analyzed using LSDA. This plot shows that the both spin states of the Si DB are below the Fermi level, and thus the Si DB is doubly occupied. **(d)** Even with U and $U+V$ corrections, the Si DB remains doubly occupied. The BCH state is consistently ~ 0.5 eV higher than the Si DB.

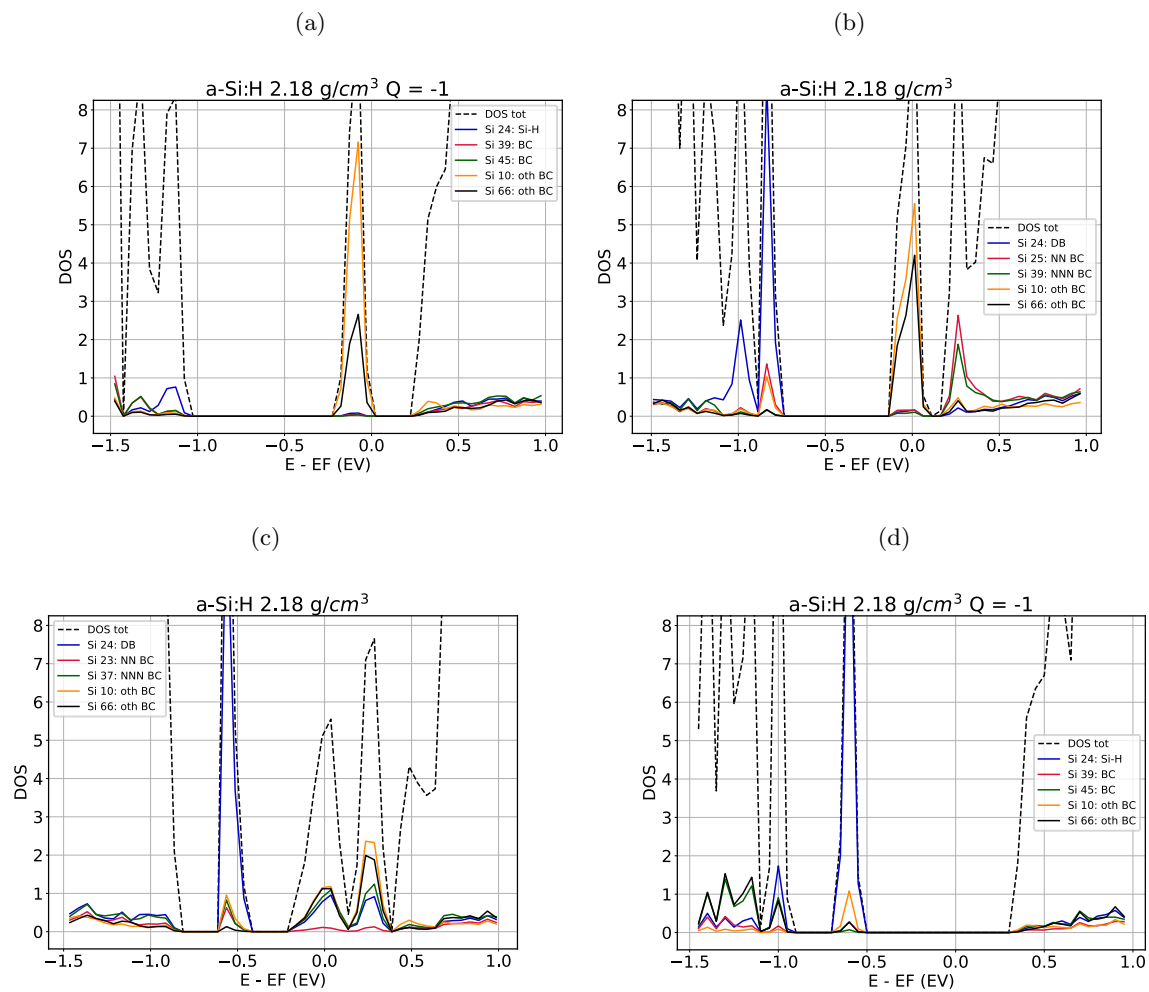


FIG. 3: PDOS from one of the $a\text{-Si:H}$ cells showing the variability in the energy of the Si DB state and the BCH state within the bandgap.